# Generation of the jovian radio decametric arcs from the Io Flux Tube

Sébastien L. G. Hess, Fabrice Mottez, Philippe Zarka, Thomas Chust

## To cite this version:

Sébastien L. G. Hess, Fabrice Mottez, Philippe Zarka, Thomas Chust. Generation of the jovian radio decametric arcs from the Io Flux Tube. Journal of Geophysical Research Space Physics, 2008, 113, pp.3209. 10.1029/2007JA012745 . hal-03786567

JOURNAL OF GEOPHYSICAL RESEARCH, VOL. 113, A03209, doi:10.1029/2007JA012745, 2008

# Generation of the jovian radio decametric arcs from the Io Flux Tube

S. Hess,[1,2] F. Mottez,[1] P. Zarka,[2] and T. Chust[3]

Received 22 August 2007; revised 6 November 2007; accepted 13 December 2007; published 20 March 2008.

[1] Jupiter's radio emissions are dominated in intensity by decametric radio emissions due to the Io-Jupiter interaction. Previous analyses suggest that these emissions are cyclotron-maser emissions in the flux tubes connecting Io or Io's wake to Jupiter. The electrons that trigger the emission are thought to be accelerated toward Jupiter. We present simulations of this hot electron population under the assumption of impulsive acceleration, consistent with the accelerated electron populations seen in the Io's wake by Galileo during its flyby in 1995. After the impulsive acceleration phase, the electrons are supposed to have an adiabatic motion along the magnetic field lines. Near Jupiter, a loss cone and a shell appear in the magnetically mirrored electron population. Such features are able to amplify extraordinary (X) mode radio waves. We compute the X-mode growth rate, which allows us to build theoretical dynamic spectra of the resulting Jovian radio emissions. The study of the growth rates obtained by simulation and their comparison with ground-based radio observations provide strong constraints on the acceleration process and energy sources at the origin of the Io-controlled decameter emissions.

**Citation:** Hess, S., F. Mottez, P. Zarka, and T. Chust (2008), Generation of the jovian radio decametric arcs from the Io Flux Tube, *J. Geophys. Res.*, *113*, A03209, doi:10.1029/2007JA012745.

## 1. Introduction

[2] The motion of the Jovian satellite Io across magnetic field lines, within the Io Plasma Torus (IPT) surrounding its orbit, provides an important and continuous energy source for electron acceleration, ultimately generating intense decametric radio emissions [*Queinnec and Zarka*, 1998] and bright UV spots at the Io flux tube (IFT) footprints [*Prangé et al.*, 1996]. The electric field generated by this motion is thought to induce electric currents and/or Alfvén waves [*Saur et al.*, 2004] which may both accelerate electrons of the IPT and of the IFT. Because of the magnetic mirror effect near the Jovian ionosphere, the distribution of these electrons becomes unstable and causes wave amplification near the local cyclotron frequency. Many instabilities have been invoked to describe the emission mechanism. A discussion of these generation processes is given by *Zarka* [1998] and references therein. In the present paper we investigate the role of the Cyclotron-Maser Instability (CMI) [*Wu and Lee*, 1979; *Wu*, 1985] which has a high efficiency and seems to be relevant for most of the planetary auroral radio emissions.

[3] Io-controlled decameter emissions mainly appear as arcs on the dynamic spectra recorded from the ground (Figure 1) or from space [*Boischot et al.*, 1981; *Leblanc*, 1981]. Assuming that this arc shape is due to Jovian magnetic field topology combined with source-observer geometry (emission is detected only when the observer is illuminated by the very anisotropic beaming pattern of the radio source), *Queinnec and Zarka* [1998] showed that radio arcs correspond to emissions from an "active" set of magnetic field lines whose longitude is few tens of degrees less than Io's, in the downstream direction, and put constraints on the radio beaming of the source: The arc emission corresponds to a beaming at 60° to 80° from the direction of the magnetic field in the source (i.e., a hollow conical beam). Figure 2a shows the beaming angle of a typical Io-B arc (the one displayed on Figure 1) as measured by *Queinnec and Zarka* [1998] assuming a lead angle of 30° between the IFT and the active field line, and in the frame of the VIP4 Jovian field model [*Connerney et al.*, 1998]. Figure 2b plots the same beaming angle as in Figure 2a versus the altitude of the source (assuming an emission at the local electron cyclotron frequency $f_{ce}$). The high frequency part of the arc (thick solid line) and its weak tail (dashed line) are emitted close to the Jovian surface. This was already visible in Figure 3, adapted from [*Queinnec and Zarka*, 1998]. These authors also discussed the possibility of a variable lag along the arc and especially its weak tail, that would cause it to be produced entirely at the Jovian surface (dotted arc of Figure 3). For the present study, the relevant information that we will compare to our simulation results is the decrease of the beaming angle observed when the sources gets close to the ionosphere (thick solid line), as compared to its near constancy at higher altitudes (e.g., in the range 17–28 MHz). The slight decrease of the beaming angle below 17 MHz is due to propagation effects, inde-

---

[1] LUTH, Observatoire de Paris, CNRS, Université Paris Diderot, Meudon, France.

[2] LESIA, Observatoire de Paris, CNRS, UPMC, Université Paris Diderot, Meudon, France.

[3] CETP - IPSL/CNRS, Vélizy, France.

0148-0227/08/2007JA012745

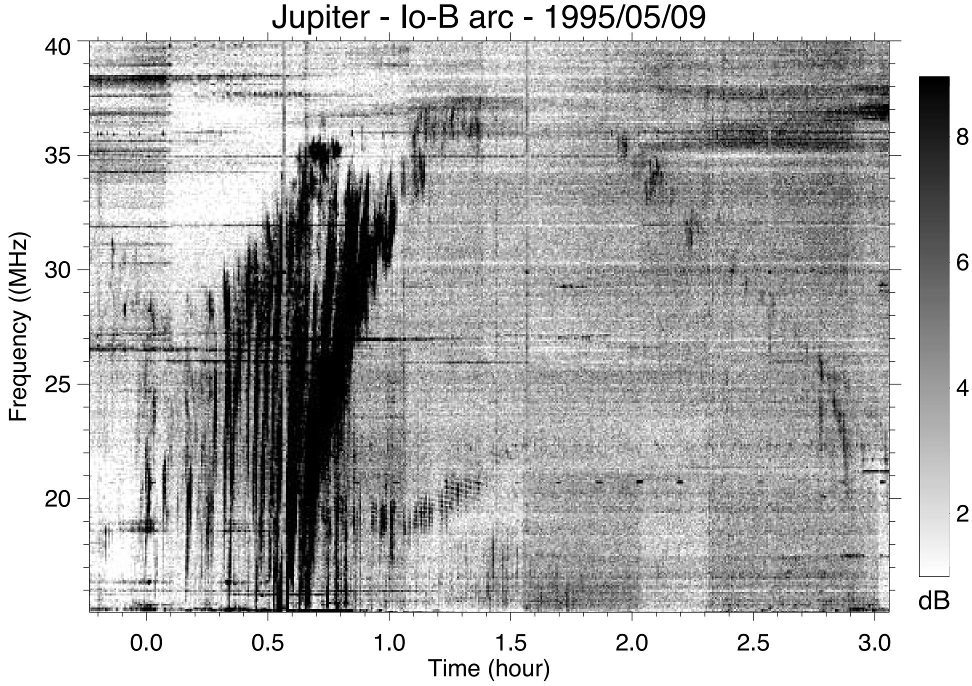

**Figure 1.** Dynamic spectrum of a typical Io-controlled arc. This is a so-called Io-B arc, recorded for an observers Jovian longitude of 150° ± 50° and a phase of Io (counted positively in the direct sense from the anti-observer direction) of 100° ± 10°. The radio emission is right-hand elliptically polarized and corresponds to X mode emission from the northern hemisphere (the weaker structure between 1.0 and 1.5 h and 19–22 MHz is a left-hand arc emission from the southern hemisphere). Horizontal lines are interference. The main part of the arc (0.6–1.0 h, 15–36 MHz) is preceded by fringes and followed by a weak tail with decreasing frequency. This arc was studied by *Queinnec and Zarka* [1998]. Emission comes from an active (set of) field line(s) moving along with Io. The emission detected from 0.8 h and after comes from a source close to the Jovian ionosphere.

pendent of the radio emission generation process, which will be discussed in a future work. According to CMI theory, the radio beaming is controlled by the phase space distribution of the electrons. Which kind of mechanism can generate a distribution consistent with the observed radio beaming, and thus with the observed radio arcs?

[4] Galileo's flyby of Io in 1995 showed several kinds of electron distributions corresponding to different sources of electron acceleration, in particular heated electrons and beams caused by parallel accelerations [*Frank and Paterson*, 1999].

[5] Our purpose is to simulate electron acceleration along the IFT due to a time-limited heating (corresponding to the sweeping of Io by the corotating plasma of the IPT); we compute the electron distribution along the IFT resulting from time-of-flight effects and the CMI growth rates from this distribution, in order to determine the radio signature of the different kinds of acceleration. The cyclotron maser emissions observable outside the source occur on the L-O (left handed polarization) or R-X (right handed polarization) modes. The observations of the Jovian radio emissions show that the R-X mode is dominant. So we must produce emissions on the R-X mode. A similar simulation has been performed in the case of an acceleration by Alfvén waves in the IFT, resulting in the generation of radio bursts with short timescale similar to the Jovian S-bursts [*Hess et al.*, 2007].

[6] We use a test particle code to compute electron distribution along the IFT. The particle motion and the way they are injected and accelerated are described in section 2. CMI growth rate computation is discussed in section 3. Results are presented in section 4 and are discussed and compared to the observational data in section 5.

## 2. Description of the Simulation

### 2.1. Electron Motion

[7] We simulate the motion of electron guiding-centers in imposed (not self-consistent) magnetic and gravitational fields. The equation of motion is given by the conservation of the magnetic moment $\mu$ and by the gradient of the gravitational (and inertial) potential $\phi_G$.

$$\mu = v_\perp^2/B = const. \tag{1}$$

$$\frac{dv_{//}}{dt} = -\nabla_{//}(\mu B + \phi_G) \tag{2}$$

[8] The permanent magnetic field is computed using the VIP4 multipolar magnetic field model of Jupiter [*Connerney et al.*, 1998]. This model was built from in situ magnetic field measurements of Voyager and Pioneer, and from infrared observations of the position of the IFT footprints on Jupiter. Up to now, this it is the most accurate published model for the computation of the magnetic field in or near the IFT.

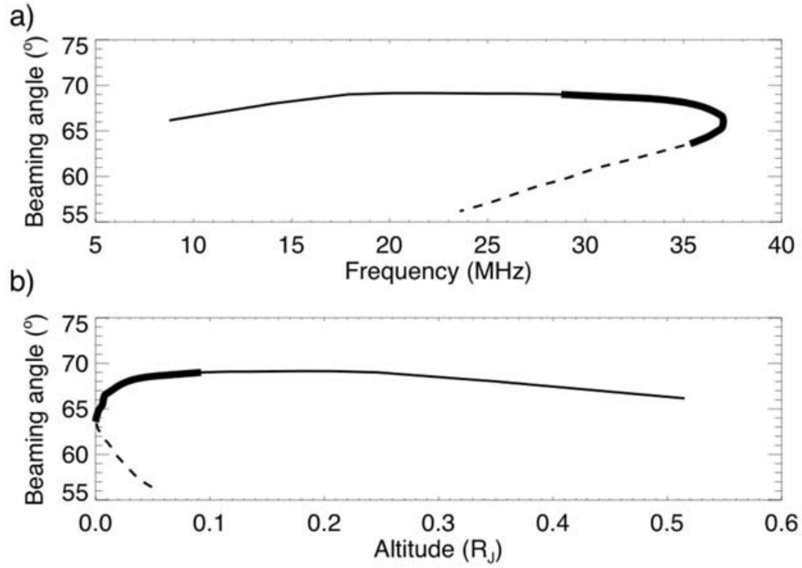

**Figure 2.** (a) Beaming angle of the Io-B arc of Figure 1 versus frequency, assuming a lead angle of 30° between the IFT and the "active" field line (VIP4 magnetic field model is used). (b) Same beaming angle versus altitude of the source (assuming an emission at $f_{ce}$). The thick solid line emphasizes the emission produced <0.1 RJ above the ionosphere, which will provide the major constraint to be compared to our simulations: the beaming angle decreases with the source altitude. The dashed line is the weak arc tail produced close to the ionosphere, and possibly at the ionosphere if the lead angle is allowed to vary along the arc [see *Queinnec and Zarka*, 1998; Figure 3]. We will not consider this tail as a constraint for the present work.

[9] Io-controlled Jovian radio emissions occur only when Io's longitude lies in a specific range of about 160° to 300° (so called "active" longitudes) [*Carr et al.*, 1983; *Queinnec and Zarka*, 1998]. We choose here to simulate the magnetic field line in northern hemisphere whose longitude at equator is 230° (i.e., the median value of the above range). This value corresponds to the so-called "Io-B" and "Io-A" emissions which are the strongest sources of Io-controlled emissions.

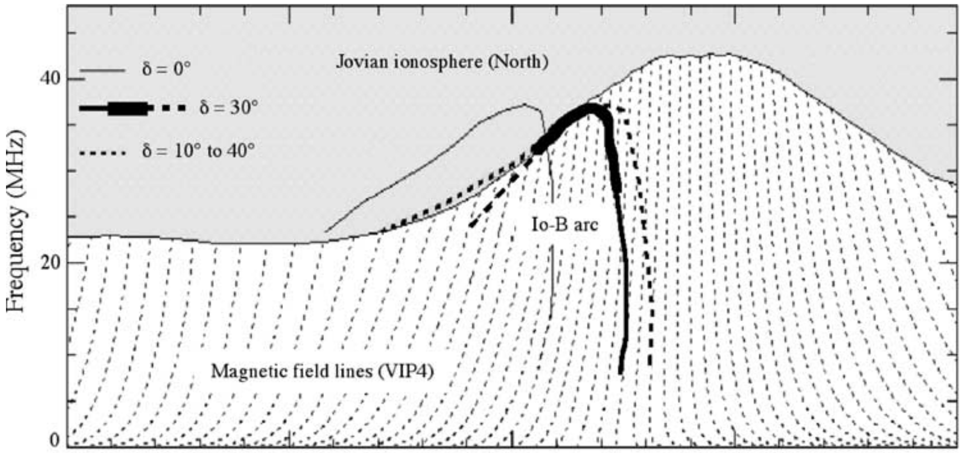

**Figure 3.** Peak lines of the Io-B arc of Figures 1 and 2 versus longitude of source field lines and gyrofrequency along them. Dotted lines represent Jovian field lines (VIP4 model), with 5° spacing at the equator. Along the arc, radio emission is detected as a function of frequency and time, or equivalently as a function of frequency and Io's longitude. The corresponding field line is followed up to the level where the gyrofrequency is equal to the observed frequency. The deduced radiosource locations are plotted here for constant lags $\delta = 0°$ (thin solid lines) and $\delta = 30°$ (thick solid/dashed line), as well as for a variable lag $\delta = 10°$ to 40° along its weak tail (dotted line). In the latter case, emission precisely tangents the surface gyrofrequency at the northern IFT footprint (separatrix between white and shaded regions) along the whole tail.

[10] The gravitational (and inertial) potential $\phi_G$ is given by the Jovian attraction and the centrifugal potential. Io's attraction is neglected. Thus:

$$\phi_G = \frac{GM_J}{R} + \frac{\Omega^2 R^2}{2} \tag{3}$$

where $M_J$ is Jupiter's mass, $\Omega$ is Jupiter's angular rotation rate and $R$ the jovicentric distance.

[11] In our simulation (and figures) positive velocities stand for particles moving toward Jupiter.

### 2.2. Evidence for Energetic Electrons

[12] Electron distributions measured in the IPT by Voyager and Galileo [*Bagenal*, 1994; *Moncuquet et al.*, 2002] can be modeled as the sum of two populations. The cold component has a temperature of ~5 eV. The warm component has a temperature of ~200 eV. In this study we are interested in the warm population only.

[13] On 7th december 1995, Galileo crossed Io's wake during its closest approach of the satellite. Its orbit was nearly equatorial and approached Io at less than 900 km. All the results of Galileo's flyby mentioned in the present paper refer to the study of *Frank and Paterson* [1999]. During the flyby, Io's longitude was about 260°, in the "active" longitude range, but corresponding to relatively weak radio emissions. The electron energy distributions in Io's wake were recorded by two electron detectors, one parallel to Galileo spin axis and thus measuring electrons perpendicular to the magnetic field, and the other perpendicular to spin axis and measuring over a wide range of pitch angles. By averaging the records of each detector over one spin period, they obtain the total energy distribution of the electrons and their perpendicular energy distribution.

[14] These records revealed two kinds of energetic electron populations: electron beams with a mean parallel kinetic energy of 800 eV and heated electrons at a temperature of 350 eV (this latter population is called hereafter the "hot" population). The beams are observed during ~0.5 min and the heating during ~2.5 min. These durations represent the time during which Galileo crossed the regions where accelerated populations are present. We note that the time required for Io to move by one diameter relative to the IPT plasma is $2R_{Io}/v_{Io} \sim 1$ min. (with $v_{Io}$ the velocity of Io relative to the torus and $R_{Io}$ the Io's radius). Thus 1 min is likely to be the characteristic duration of the Io-induced acceleration.

### 2.3. Particle Injection

[15] We simulate only the warm and energetic (hot or beam) components of Io's electron population and we neglect the cold (5 eV) population. Before accelerated electrons are injected into the test particle simulation, the IFT is filled with electrons with a maxwellian distribution and a temperature of 175 eV, consistent with the temperature of the electron halo measured by Voyager and Galileo.

[16] During the simulation, a constant number of warm particles (~700 at each time step) is injected into the 1D simulation box at Io's boundary. The particles can exit the simulation at both ends of the grid, simulating thus loss by collision in the dense Jovian ionosphere or IPT. Our simulation is made with about $6.4 \times 10^7$ particles on a 4096 cells grid.

[17] When the simulated IFT is filled with a warm plasma, we inject an accelerated electron distribution at the upper (Io) boundary, for a duration of 5 s. This duration may be far less than the actual duration of the acceleration by Io, but it is sufficient to allow us to simulate the transition phases. The duration of the acceleration does not change the evolution of the distribution gradient involved in the radio emission (see below). Longer acceleration just adds a phase during which the electron distribution remain constant in the phase space and thus causes a constant emission amplification.

[18] Both kinds of acceleration seen by Galileo (heating and beams) are taken into account in this paper. The introduction of accelerated particles at the Io boundary (i.e., the center of the IPT) does not mean this is the place where the accelerations occur, but the place where the measurements are done by Galileo (i.e., where such accelerated distributions are observed). In fact the accelerations may occur away from the torus. Heating may occur on the "borders" of the IPT where Alfvén waves may filament and interact more strongly with the particles [*Chust et al.*, 2005], and beams seem to be anti-planetward beams generated near Jupiter [*Williams et al.*, 1999; *Mauk et al.*, 2001].

## 3. Cyclotron-Maser Growth Rate

### 3.1. Resonance and Growth Rate

[19] A review of the linear Cyclotron Maser Instability (CMI) theory is presented by *Wu and Lee* [1979], *Wu* [1985] and *Galopeau et al.* [2004]. The latter authors deduce the Io "active" longitudes from the CMI combined with Jupiter's magnetic field geometry. CMI emission is produced by electrons which fulfill the wave-particle resonance condition:

$$\omega = \omega_c/\Gamma - k_{//}v_{//} \tag{4}$$

where $\omega$ is the wave real frequency, $k$ its wave vector, $\omega_c$ the electron cyclotron frequency, $v$ the resonant particle velocity and $\Gamma$ the relativistic Lorentz factor. In the weakly relativistic approximation the wave-particle resonance condition is represented in the velocities plane ($v_{//}$, $v_\perp$) by a circle of center $v_0$ and radius $v_R$ given by:

$$v_0 = -\frac{k_{//}c^2}{\omega_c} = -cN\frac{\omega}{\omega_c}\frac{\mathbf{k}.\mathbf{b}}{k} \simeq -c\frac{\mathbf{k}.\mathbf{b}}{k} = -c\cos\beta \tag{5}$$

$$v_R = \sqrt{v_0^2 - 2c^2(\frac{\omega}{\omega_c} - 1)}. \tag{6}$$

where $\mathbf{b}$ is the magnetic field unit vector, $\beta$ is the radio beaming angle relative to the magnetic field in the source and $N$ the refraction index ($\simeq$1). We assume $\omega \simeq \omega_c$ in equation 5. The CMI growth rate $\gamma$ for a given resonance circle of radius $\mathbf{v_R}(\theta)$, with $\theta$ counted from the parallel velocity axis, is obtained by integration along this resonance circle of the particle distribution gradient relative to the perpendicular velocity $\nabla_{v_\perp} f(\mathbf{v}_0, \mathbf{v}_\mathbf{R}(\theta))$. The imaginary part of the solution of the right handed mode dispersion equation in the cold plasma approximation and for $|\omega| > |\gamma|$ is:

$$\gamma = \frac{\omega_p^2 c^2}{8\omega_c} \int_0^{2\pi} v_\perp^2(\theta) \nabla_{v\perp} f(\mathbf{v}_0, \mathbf{v}_\mathbf{R}(\mathbf{q})) d\theta \qquad (7)$$

where $\omega_p$ is the electron plasma frequency. The R-X mode (right handed mode observable outside the source) occur only above a low cutoff frequency ($\omega_x > \omega_c$ in the cold plasma approximation). The cold plasma approximation is used here, although we simulate warm plasma, because of the probable presence of a dominant cold (~0.3 eV) ionospheric plasma population in the emission region. This population has been estimated to be denser than the warm Iogenic plasma by several orders of magnitude in a large part of the emission region [*Su et al.*, 2003]. Thus the dispersion equation used to obtain the above solution (equation (7)) is valid only for emissions at frequencies above the electron cyclotron frequency. A more accurate value can be obtained by using a relativistic multiplicative factor which represents the warm-to-ionospheric population density ratio [*Omidi et al.*, 1984]. As this factor has almost the same value for all the amplified modes, we can directly compare these modes without computing the relativistic correction. However, *Omidi et al.* [1984] do not consider any variation of the cutoff frequency induced by the presence of the warm population which could permit R-X mode amplification below $\omega_c$ (thus the emissions at frequencies lower than the cold plasma cutoff frequency are on the Z mode which cannot propagate out of the plasma and is not observable from the Earth).

[20] Positive growth rates require a positive gradient $\nabla_{v_\perp} f(\mathbf{v}_0, \mathbf{v}_\mathbf{R}(\theta))$ with a dominant contribution to the integral in equation (7). This can be obtained with "loss cone" and "shell" distributions (Figure 4a). In our simulation we compute from the particle distribution, at several points along the field line, the growth rates for several resonance circles defined by their center $v_0$ and radius $R$ (which correspond to several frequencies $\omega$ and parallel wave vectors $k_{//}$). Each resonance circle corresponds to a different mode. The observed mode is the mode with the largest growth rate since it is the most amplified. In this paper we consider two main classes of instabilities:

[21] The oblique instability. We consider modes tangent to the loss cone border, i.e., the characteristics of the emissions (relation between beaming angle, resonant particle velocity and local magnetic flux for example) are the same than for the loss cone instability. However, the energy source can be different from the loss cone distribution, for example be a ring or a shell distribution.

[22] The perpendicular instability. We consider modes whose resonance circle center $v_0$ corresponds to a null velocity. Then the emission occurs perpendicularly to the magnetic field lines.

[23] The growth rates of these instabilities are computed separately since their emission characteristics are quite different (beaming angle, propagation, ...).

## 3.2. Oblique Instability

### 3.2.1. Beaming Angle

[24] In the case of the oblique instability, equation (7) can be solved analytically. Since the resonance circle is tangent to the loss cone border the integral reduces to:

$$\gamma = \frac{\omega_p^2 c^2}{8\omega_c} v_{\max,\perp}^2(\theta_{loss\ cone}) \nabla_{v_\perp} f(\mathbf{v}_{\max}, \mathbf{v}_\mathbf{R}(\theta_{loss\ cone})) \qquad (8)$$

where the resonant particle velocity $\mathbf{v}_{\max}$ maximizes the growth rate $\gamma$. Remembering that $v_0 = c\cos(\beta)$ (equation (5)), we can write the beaming angle as a function of the loss cone angle $\alpha$, or equivalently as a function of the emission frequency $f$ and the frequency at the jovian "surface" $f_{\max}$ as:

$$\cos\beta = v_{\max}(c\cos\alpha)^{-1} = v_{\max}\left(c\sqrt{1 - f/f_{\max}}\right)^{-1} \qquad (9)$$

### 3.2.2. Oblique Instability in Presence of a Shell

[25] When the distribution is composed of both a shell and a loss cone (like the two distributions of Figures 4a and 4e) the resonance circle of the oblique instability can be tangent to the core (warm particles) or to the shell (hot/accelerated particles), inducing radio emissions with different growth rates and beaming angles. The oblique instability growth rate depends mainly on the density in the phase space and on the perpendicular velocity of the electrons at the point of the resonance circle tangent to the loss cone border. Even if the perpendicular velocity of the shell is larger than the core thermal velocity, the resonance circle of the most unstable mode can be tangent to the core if the density of electrons in the shell is too low. There is a density threshold below which the emissions are mainly due to the core electrons. The threshold value of the shell density $n_{shell}$ may be estimated from equation (8) as:

$$\frac{n_{shell}}{n_{core}} \sim \frac{v_{\max}^2 f_{core}(v_{\max}, \alpha)}{v_{shell}^2 f_{shell}(v_{shell}, \alpha)} \qquad (10)$$

where $f_{core}(v, \alpha)$ and $f_{shell}(v, \alpha)$ are the values of the velocity distribution function of the core and of the shell along the loss cone border ($\alpha$ is the loss cone aperture), $n_{core}$ is the core density and $v_{shell}$ the shell typical velocity (radius). Considering $f_{core}$ as a maxwellian distribution with thermal speed $v_{T,core}$ and $v_{\max} = \sqrt{3/2}\, v_{T,core}$, we estimate the shell density threshold as:

$$\frac{n_{shell}}{n_{core}} \sim \frac{3v_{T,core}}{\sqrt{8\pi} v_{shell}^2} \frac{\exp(-3/2)}{f_{shell}(v_{shell}, \alpha)} \qquad (11)$$

## 3.3. Perpendicular Instability

[26] The perpendicular instability has a solution to the resonance condition (equation (4)) for $v_{//} = 0$, implying $\omega < \omega_c$. However, in the emission region the dominant species is the ionospheric plasma whose temperature is less than 1 eV, thus the cold plasma approximation is valid and imposes a cutoff frequency slightly higher than $\omega_c$. It implies that the perpendicular emission should occur at frequencies lower than the cold plasma cutoff frequency. Hot plasma terms in

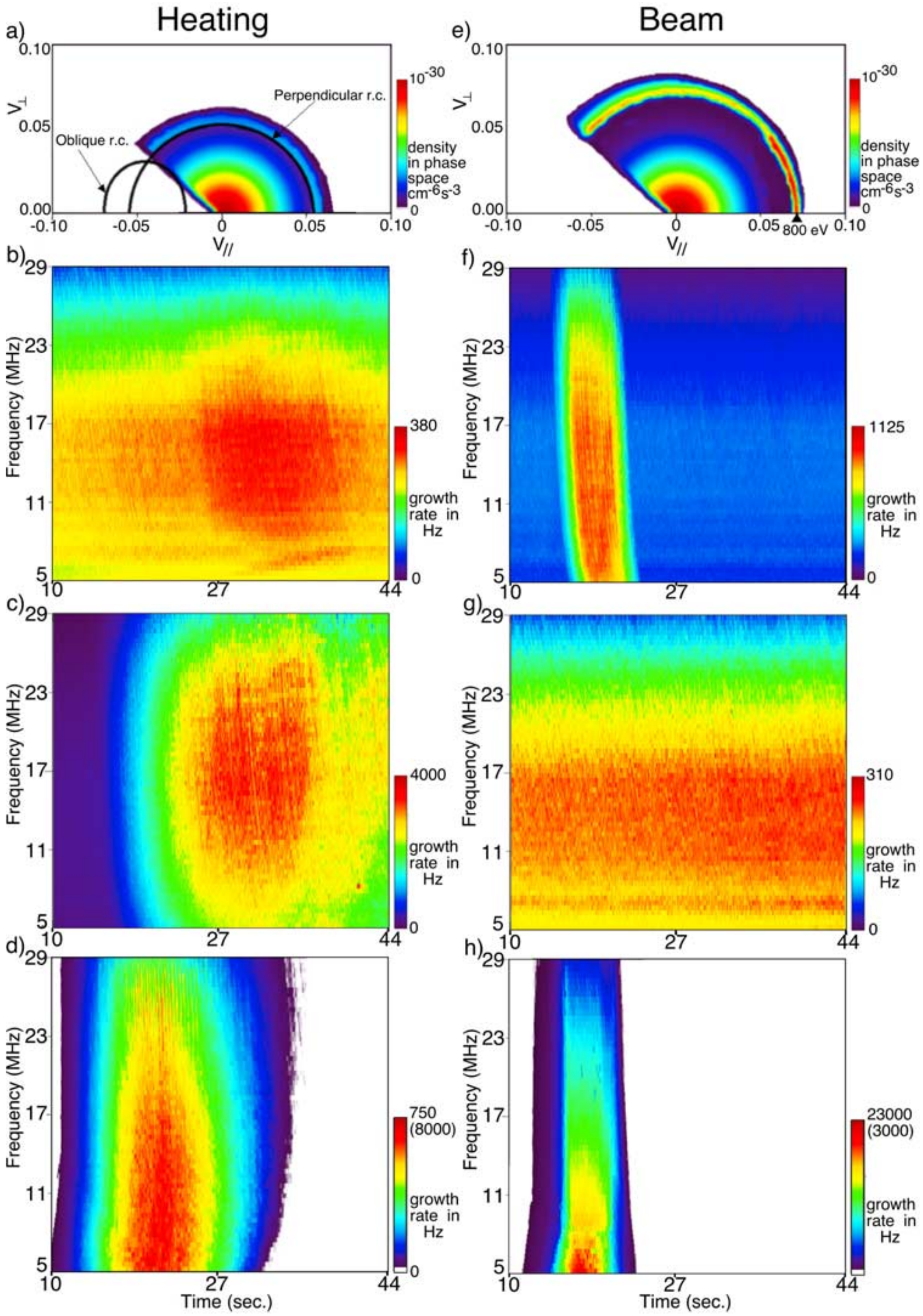

**Figure 4.** (a) Electron distribution in the heating case at an altitude of 0.25 $R_J$ and at time t = 30 s after injection. The core of the distribution is composed of warm (175 eV) electrons. The ring of particle is formed by the hot electrons due to particle time-of-flight and magnetic mirroring effect. (b) Dynamic spectra of the oblique instability: heating with a hot/warm density ratio equal to 1. (c) Dynamic spectra of the oblique instability: heating with a hot/warm density ratio equal to 10. (d) Dynamic spectra of the perpendicular instability: heating. The growth rate value is given for a hot/warm density ratio of 1 and of 10 (latter in parenthesis). (e) Electron distribution in the electron beam case at an altitude of 0.25 $R_J$ and at time t = 20 s after injection. The ring is composed of accelerated particles with a mean energy of 800 eV. (f) Dynamic spectra of the oblique instability: beam with a beam/core density ratio equal to 1. (g) Dynamic spectra of the oblique instability: beam with a beam/core density ratio equal to 0.1 (h) Dynamic spectra of the perpendicular instability: beam. The growth rate value is given for a beam/core density ratio of 1 and of 0.1 (latter in parenthesis).

the R-X mode dispersion relation may reduce this value of the cutoff frequency, but they are not taken into account here since there is no analytical solution for it [*Pritchett*, 1984]. Consequently the growth rate in equation (7) actually corresponds to the growth rate of the Z-mode ($\omega < \omega_c$), which cannot propagate in vacuum (and therefore cannot be observed from the Earth), and not to the R-X mode. An observable (R-X mode) perpendicular emission can be obtained with an hot plasma correction or by mode conversion (upon the density gradients), but in both cases the overall efficiency of the process and thus the amplitude of the observable emission are not known.

[27] Therefore equation (7) is not accurate (actually not valid) for a perpendicular emission observable by remote sensing. Nevertheless we use it to estimate approximate observable perpendicular wave (R-X) amplification rates, although the exact observable perpendicular wave amplification rates should be lower than those computed with this equation since they strongly depend on the density ratio of the hot (emitting) versus cold (dominating in density) electron populations [*Pritchett*, 1984].

[28] We note that in situ measurements could show a dominant Z mode in the region of emission, even if it might not result in a dominant perpendicular emission observable by remote sensing (R-X mode).

## 4. Results

### 4.1. Simulation With Electron Heating

[29] We first simulate the injection of isotropic energetic (hot) electrons. The temperature of the electron distribution injected at Io's wake boundary is increased by a factor 2 (from 175 eV to 350 eV) during 5 s.

[30] Figure 4a shows the distribution of the electrons at an altitude of 0.25 $R_J$ above the Jovian ionosphere at a time t = 30 s after the injection. The core of the distribution is composed of non-heated (warm) electrons, still present due to their long time of flight from Io's wake. This part of the distribution is purely maxwellian except for an empty range of pitch angle, the so-called "loss cone", generated by the collisional loss in the Jovian ionosphere of the particles with lowest pitch angles. Particles with larger pitch angles are reflected at higher altitudes by magnetic mirror effect.

[31] The shell in the velocity distribution is created by the heated electrons, through the combined effects of particle time-of-flight and magnetic mirroring. Heated electrons whose parallel velocity at Io's boundary is very large have already passed at the location of Figure 4a and are not present anymore. Those whose parallel velocity is low have a longer time-of-flight and have not yet arrived. The other particles constitute the shell in the velocity distribution.

[32] The inner radius of this shell decreases with time as less energetic particles, with a longer time-of-flight, reach the altitude of 0.25 $R_J$ above Jupiter. Meanwhile the outer radius decreases too, as all the particles with short time-of-flight are already gone. Thus heating generates a shell distribution above the Jovian ionosphere, whose radius decreases with time.

[33] In terms of CMI, the radius of the resonance circle for the perpendicular instability, and possibly that of the oblique instability, must decrease too. This has implications in term of the growth rate value since in equation (7) the perpendicular energy term ($v_\perp^2(\theta)$) decreases and the gradient ($\nabla_{v_\perp} f(\mathbf{v}_0, \mathbf{v_R}(\theta))$) changes. Moreover, in the case of an oblique emission, the variation of the resonant circle corresponding to the most unstable mode changes the beaming angle (equation (9)). Because of the time that the particles need to travel to Jupiter and come back to the altitude of emission, the radius of the shell varies with the pitch angle (the radius for reflected particles is larger than for planetward particles). This implies that higher growth rates may be found with perpendicular instability resonance circles not centered over $v_{//} = 0$, in particular at low frequency (high altitude and thus longer time-of-flight). We can thus infer that the beaming angle of the perpendicular instability decreases slightly at low frequency.

[34] Figure 4b shows the dynamic spectrum of the oblique instability growth rates and Figure 4d those of the perpendicular instability growth rates. As the warm population has a loss cone distribution even in the absence of acceleration by Io, the oblique instability present a constant background (which reach the maximum value of ~300 Hz in the 11 MHz to 17 MHz frequency band). On the contrary, there is no shell or ring distribution without acceleration by Io, consequently there is no background growth rates for the perpendicular instability.

[35] On both figures the increase of the growth rate due to the heating (between 10 s and 30 s after injection for the perpendicular emission, from 25 s to >44 s for the oblique one) persists on a time much longer than the heating duration itself (5 s). This is due to the different time-of-flight of the particles, depending on their kinetic energies.

[36] The decrease of the growth rate with time due to the resonance circle radius decrease is visible on the perpendicular growth rate dynamic spectrum (Figure 4d after 22 s).

[37] The oblique instability growth rate begins to increase several seconds after that of the perpendicular instability (at t ~ 12 s for the perpendicular emission (Figure 4d) and at t ~ 25 s for the oblique one (Figure 4b)). The oblique instability seems thus to be little efficient at the time when the shell radius is large (i.e., for the most energetic particles). This is due to the low density of the heated particles, which do not generate a growth rate larger than the warm population until the density of particles in the shell reach a sufficient value (cf. section 3.2.2).

[38] In the particle distributions observed by Galileo, the heating occurs simultaneously with an increase of the density by more than one order of magnitude, Therefore we made another run where we multiply the density of the injected particles by ten during the 5 s heating. Figure 4c shows the resulting dynamic spectrum of the oblique instability growth rate. The increase of the oblique instability growth rate begins only few seconds after that of the perpendicular instability (at t ~ 12 s for the perpendicular emission (Figure 4d) and at t ~ 16 s for the oblique one (Figure 4c)) and lasts for a longer time. We can see structures drifting in the time frequency plane appearing on Figure 4c. Each of them is produced by a bunch of electrons (in phase space) whose motion causes the observed drift. However, their discreteness is only a consequence of the low number of particles used in our simulation.

[39] Figures 5a and 5b show the variations of the oblique instability beaming angle versus time and frequency. The beaming angle depends on the energy of the emitting

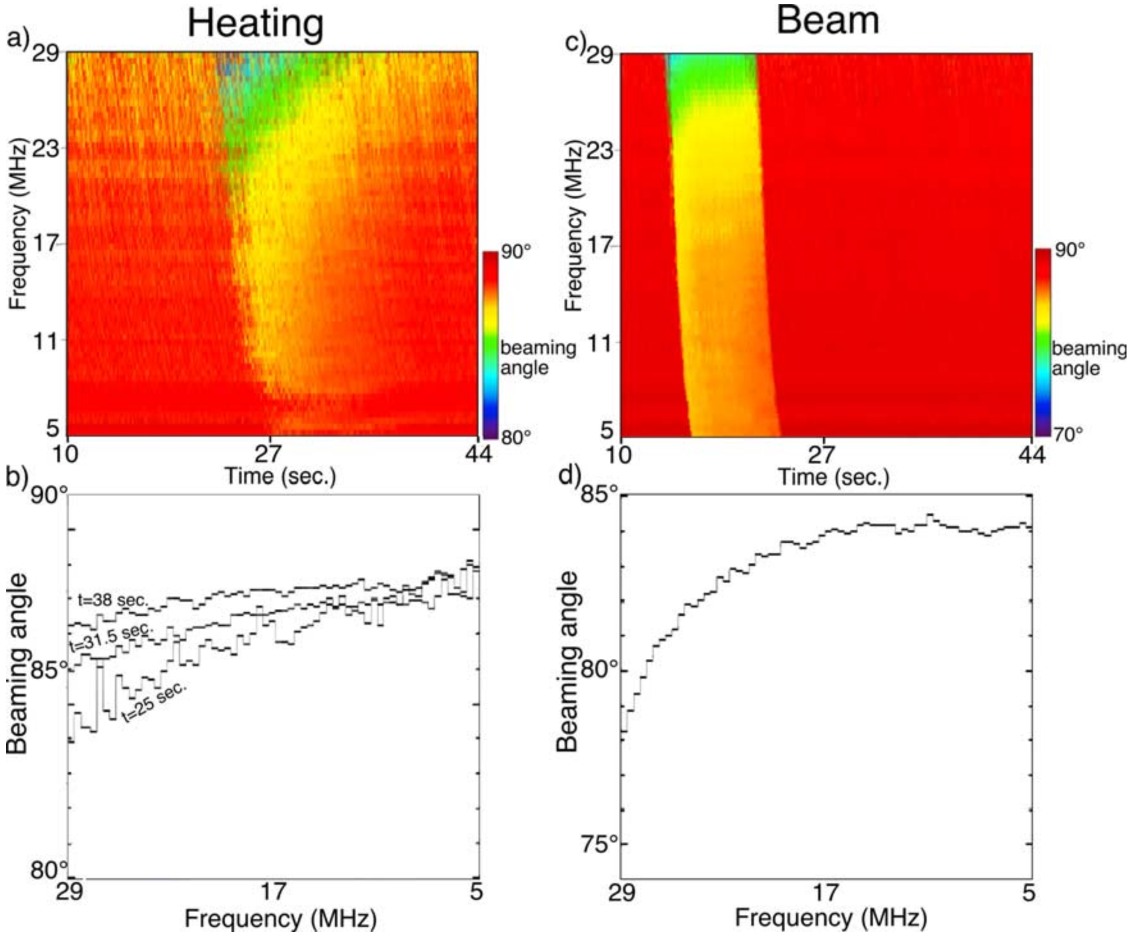

**Figure 5.** Dynamic spectra of the beaming angle of the oblique instability. (a) Heating: The beaming angle value is given in the case of a hot/warm density ratio of 1. (b) Vertical profile of the latter dynamic spectrum (Figure 5a) at time = 25, 31.5, and 38 s. The beaming angle profile decrease s toward high frequencies and evolves over time (c) Beam: The beaming angle value is given in the case of a beam/core density ratio of 1. (d) vertical profile of the latter dynamic spectrum (c) at time = 17 s.

electrons, consistent with equation (9). As the radius of the shell of electrons decreases with time, the electron energy and beaming angle decrease too. The beaming angle decreases more steeply at the highest frequencies (close to the Jovian ionosphere). This is particularly visible during the maximum of the amplification (t = 25 s to t = 35 s). When the energy is low, the decrease occurs for frequencies close to the surface cyclotron frequency (32 MHz in our case).

### 4.2. Simulation With Electron Beams

[40] The second type of acceleration that we have simulated corresponds to the electron beams accelerated parallel to the magnetic field, which have been observed by Galileo. We impose a localized electric potential difference of 800 V at the injection edge of the simulation grid in order to accelerate the electrons during 5 s.

[41] Figure 4e shows the distribution of the electrons at an altitude of 0.25 $R_J$ at time t = 20 s after injection. The shell, whose radius remains constant during the simulation as expected, corresponds to particles with a mean energy of 800 eV. The shell density is larger than in the heating case since the whole distribution is accelerated and the accelerated distribution is centered around a maximum at 800 eV (Figure 4e).

[42] Figure 4f shows the dynamic spectrum of the oblique instability growth rate. Contrary to the heating case, the growth rate increases as the first accelerated electrons reach the emission region and persists less than 7–8 s (roughly equal to the acceleration duration). The time-of-flight effect is less important in this case since the velocity dispersion of the electrons is smaller.

[43] Figure 4h shows the dynamic spectrum of the perpendicular instability growth rate. It has almost the same characteristics than in the heating case, except that the duration of the radio emissions is longer (∼10 s), but still less than twice the acceleration duration. Moreover, the shell characteristics (density, radius) do not change during the passage of the accelerated electrons, thus the growth rate remains approximately constant.

[44] Figure 5c shows the dynamic spectrum of the beaming angle associated with the oblique instability. Since the particles are more energetic than in the heating case the beaming angle is lower (Figure 5d). Contrary to the heating case, in which the characteristics of the shell change with time (density increase and radius decrease), these parame-

ters remain almost constant in the electron beam case, thus the radio beaming angle remains constant during the whole passage of the accelerated particles. Shorter radio emission duration and constant beaming angle are the main measurable differences with the heating case, which can be checked against observations of an Io induced radio arc.

[45] Both oblique and perpendicular instabilities growth rates are larger in the electron beam case than in the heating case (without density increase). The larger growth rate for the oblique instability is mainly due to the energy of the particles (about twice larger in the electron beam case) and, for a more limited part, to the larger electron density in the shell. The perpendicular instability growth rate is about 30 times larger in the electron beam case than in the heating case. This is not only due to electron energy and to the electron density in the shell, but also to the lower density (lower gradient) of warm particles of the core at 800 eV than at 350 eV, steepening the perpendicular gradient of the distribution. As the beam is obtained by an acceleration of the whole warm electron distribution, its density (in space) is equal to that of the warm core. We may have overestimated by one order of magnitude the density of the electron beam, compared to the Galileo measurements.

[46] The effects of a lower density of the accelerated electrons on the oblique instability are discussed in section 3.2.2, implying that there is a beam density threshold below which there is no increase of the emissions above the background. Considering $f_{shell}$ as a maxwellian distribution centered on the beam velocity $v_{shell}$ with a thermal speed $v_{T,shell}$, the value of the beam density threshold $n_{shell}$ may be estimated following equation (11) as:

$$\frac{n_{shell}}{n_{core}} \sim \frac{3v_{T,core}}{2v_{shell}} \exp\left(\frac{(v_{shell}\sin\Omega)^2}{v_{T,shell}^2} - 3/2\right) \sim 0.16 \qquad (12)$$

with $n_{core}$ the core density and $\Omega \sim 2^\circ$ the loss cone aperture at the equator. Galileo measurements suggest that the actual $\frac{n_{shell}}{n_{core}}$ ratio is close to the threshold value, so that the oblique instability due to the beam (assuming that it operates) cannot generate growth rates noticeably larger than those generated by the warm core. Figure 4g shows the dynamic spectrum for a beam/core density ratio of 0.1 (less than the threshold), which does not show any additional emission as the beam is passing. Thus the electron beams observed in Io's vicinity may not generate detectable (i.e., above the background) radio emissions from the oblique instability, but can generate it by perpendicular instability.

## 5. Discussion

[47] Our simulations show that the electron acceleration events observed by the PLS experiment on Galileo may generate radio emissions at the local electron cyclotron frequency by four ways summarized hereafter:

[48] Perpendicular instability driven by electron beams (Figure 4h). This mechanism gives large growth rates (up to 3 kHz) but, due to low beam density and (probably) overestimated perpendicular instability growth rate, it may not be the mechanism at the origin of the Jovian arc emissions. The beaming angle of the emissions generated by this mechanism is equal to 90° over the whole frequency range.

[49] Oblique instability driven by electron beams (Figure 4g). With beam densities as low as the ones seen by Galileo this mechanism may actually not generate any strong emissions at Jupiter (except if beam density or energy depends on Io's longitude: for the Galileo observation, Io was not at a longitude where strong radio arcs are usually generated). The beaming angle varies with frequency (decreasing at high frequency) but it does not vary with time.

[50] Perpendicular instability driven by heating (Figure 4d). In our simulations, this mechanism gives the largest growth rates (up to 8 kHz) but (assuming the absence of density cavities) those are overestimated due to the absence of hot plasma corrections to the X mode dispersion relation. The beaming angle of the emissions generated by this mechanism is nearly equal to 90° over the whole frequency range but it may slightly decrease at low frequency due to time-of-flight effects.

[51] Oblique instability driven by heating (Figure 4c). The growth rates generated by this mechanism (up to 4 kHz) are about two times lower than those obtained by the previous mechanism. However, due to the overestimation of the perpendicular instability growth rates mentioned above, the oblique instability growth rates may actually dominate the production of observed radio emissions. This mechanism generates emissions with a beaming angle varying along the IFT, decreasing as magnetic field increases (Figures 5a and 5b). This decrease of the beaming angle at low altitude fully agrees with the observations.

[52] In the Earth case, auroral radio emissions cannot be produced by CMI are impossible due to a large $\omega_p/\omega_c$ ratio, except in auroral cavities in which the cold plasma is depleted. In this case the hot dispersion equation leads to a cutoff frequency lower than the cyclotron frequency. The perpendicular emission is then favored. However, in the Jovian case the $\omega_p/\omega_c$ ratio is low, permitting emissions even outside auroral cavities. In this case the oblique emission may be favored for remote sensing observations.

[53] Thus the present study favors, for Io-Jupiter arc generation, the oblique instability generated by heating as it is consistent with both ground-based radio observations and Galileo in situ plasma measurements. However, if the Jovian emission were emitted from density cavities, as it happens in the Earth auroral region, the perpendicular emission (generated by beams or by heating) would probably dominate. In this case the observed beaming angle might be obtained by refraction at the edges of the cavities.

[54] **Acknowledgments.** Wolfgang Baumjohann thanks Yi-Jiun Su and Robert Mutel for their assistance in evaluating this paper.

## References

Bagenal, F. (1994), Empirical model of the Io plasma torus: Voyager measurements, *J. Geophys. Res.*, *99*, 11,043–11,062, doi:10.1029/93JA02908.

Boischot, A., M. L. Lecacheux, M. D. Kaiser, J. K. Desch, and J. W Alexander (1981), Warwick, Radio Jupiter after Voyager - An overview of the planetary radio astronomy observations, *J. Geophys. Res.*, *86*, 8213–8226.

Carr, T. D., M. D. Desch, and J. K. Alexander (1983), Phenomenology of magnetospheric radio emissions, *Phys. Jovian Magnetosphere*, 226–284.

Chust, T., A. Roux, W. S. Kurth, D. A. Gurnett, M. G. Kivelson, and K. K. Khurana (2005), Are Io's Alfvén wings filamented? Galileo observations,, *Planet. Space Sci.*, *53*, 395–412, doi:10.1016/j.pss.2004.09.021.

Connerney, J. E. P., M. H. Acuña, N. F. Ness, and T. Satoh (1998), New models of Jupiter's magnetic field constrained by the Io flux tube footprint, *J. Geophys. Res.*, *103*(12), 11,929–11,940, doi:10.1029/97JA03726.

Frank, L. A., and W. R. Paterson (1999), Intense electron beams observed at Io with the Galileo spacecraft, *J. Geophys. Res.*, *104*, 28,657–28,669.

Galopeau, P. H. M., M. Y. Boudjada, and H. O. Rucker (2004), Evidence of jovian active longitude: 1. Efficiency of cyclotron maser instability, *J. Geophys. Res. (Space Physics)*, *109*, A12217, doi:10.1029/2004JA010459.

Hess, S., F. Mottez, and P. Zarka (2007), Jovian S burst generation by Alfvén waves, *J. Geophys. Res.*, *112*, A11212, doi:10.1029/2006JA012191.

Leblanc, Y. (1981), On the arc structure of the DAM Jupiter emission, *J. Geophys. Res.*, *86*, 8546–8560.

Mauk, B. H., D. J. Williams, and A. Eviatar (2001), Understanding Io's space environment interaction: Recent energetic electron measurements from Galileo, *J. Geophys. Res.*, *106*, 26,195–26,208, doi:10.1029/2000JA002508.

Moncuquet, M., F. Bagenal, and N. Meyer-Vernet (2002), Latitudinal structure of outer Io plasma torus, *J. Geophys. Res. (Space Physics)*, *107*(A9), 1260, doi:10.1029/2001JA900124.

Omidi, N., D. A. Gurnett, and C. S. Wu (1984), Generation of auroral kilometric and Z mode radiation by the cyclotron maser mechanism, *J. Geophys. Res.*, *89*, 883–895.

Prangé, R., D. Rego, D. Southwood, P. Zarka, S. Miller, and W. Ip (1996), Rapid energy dissipation and variability of the Io-Jupiter electrodynamic circuit, *Nature*, *379*, 323–325, doi:10.1038/379323a0.

Pritchett, P. L. (1984), Relativistic dispersion, the cyclotron maser instability, and auroral kilometric radiation, *J. Geophys. Res.*, *89*, 8957–8970.

Queinnec, J., and P. Zarka (1998), Io-controlled decameter arcs and Io-Jupiter interaction, *J. Geophys. Res.*, *103*(A11), 26,649–26,666, doi:10.1029/98JA02435.

Saur, J., F. M. Neubauer, J. E. P. Connerney, P. Zarka, M. G. Kivelson (2004), *Plasma interaction of Io with its plasma torus*, pp. 537–560, Jupiter. The Planet, Satellites and Magnetosphere.

Su, Y.-J., R. E. Ergun, F. Bagenal, and P. A. Delamere (2003), Io-related Jovian auroral arcs: Modeling parallel electric fields, *J. Geophys. Res. (Space Physics)*, *108*(A2), 1094, doi:10.1029/2002JA009247.

Williams, D. J., R. M. Thorne, and B. Mauk (1999), Energetic electron beams and trapped electrons at Io, *J. Geophys. Res.*, *104*, 14,739–14,754, doi:10.1029/1999JA900115.

Wu, C. S. (1985), Kinetic cyclotron and synchrotron maser instabilities - Radio emission processes by direct amplification of radiation, *Space Sci. Rev.*, *41*, 215–298.

Wu, C. S., and L. C. Lee (1979), A theory of the terrestrial kilometric radiation, *Astrophys. J.*, *230*, 621–626, doi:10.1086/157120.

Zarka, P. (1998), Auroral radio emissions at the outer planets: Observations and theories, *J. Geophys. Res.*, *103*, 20,159–20,194, doi:10.1029/98JE01323.

---

T. Chust, CETP - IPSL/CNRS, Vélizy, France.

S. Hess and F. Mottez, LUTH, Observatoire de Paris, CNRS, Université Paris Diderot; 5 Place Jules Janssen, 92190 Meudon, France. (sebastien.hess@obspm.fr)

P. Zarka, LESIA, Observatoire de Paris, CNRS, UPMC, Université Paris Diderot; 5 Place Jules Janssen, 92190 Meudon, France.